Characterization of AC-DBD Plasma Actuator performance under external flow: Phase-resolved body-force field estimation

Gonçalo Nuno Ferreira de Moura Coutinho
goncalo.coutinho@tecnico.ulisboa.pt

Instituto Superior Técnico, Universidade de Lisboa, Portugal

November 2019

Abstract

Velocity measurements are performed to quantify the phase-resolved forcing mechanism of an AC-DBD plasma actuator in quiescent air and under the influence of external airflow. The velocity data is acquired using a particle image velocimetry system. Insight into the time-averaged and phase-resolved body-force information is provided by the Navier-Stokes equation and vorticity-equation-based method. The power consumption and current signal are acquired to characterize the plasma-discharge events. Additionally, the power consumption measurements indicate a virtually constant power consumption for free-stream velocities up to $U_\infty = 20\,\mathrm{m/s}$. The current measurements evidenced the discharge events to be independent of the external-airflow velocity. The results indicate the Navier-Stokes approach to result in an oversimplication due to the plasma-induced pressure gradient whereas the vorticity-equation-based method yields good compliance with respect to the electrical characterization of the actuator in the presence of external airflow.

Keywords: plasma actuator, discharge, external airflow, time-averaged, phase-resolved

1. Introduction

The dielectric-barrier-discharge (DBD) plasma actuator have shown promising features which are suitable for active flow control (AFC) [1]. The oscillating behaviour of the discharge is found to successfully delay the laminar-to-turbulent transition and manipulate turbulent boundary layers (BL), see e.g. [2]. In order to enhance and better understand the electrical and mechanical properties, different experimental campaigns were aimed at analysing the electrical and mechanical phenomena associated with such a device. An extensive review on the subject is provided by Corke *et al.*[3].

The main feature of the plasma actuator for AFC is the so-called 'ionic wind' which is responsible for the momentum-transfer ability to the surrounding airflow. Quantification of the plasma-induced airflow has been successfully performed in quiescent-air conditions $U_\infty = 0\,\mathrm{m/s}$ by determining the net-force production [4]. Nonetheless, the challenge of determining the body-force field is considerable. Even though two established methods either based on the Navier-Stokes equation (N.S.E.) [5] or vorticity-equation-based (V.E.) [6] are presented in literature, the body-force has only been quantified in quiescent air. For instance, Kriegseis *et al.*[4] studied the time-averaged body-force fields whilst insight into the phase-resolved force topology is provided by Benard *et al.*[7]. Both studies led to the conclusion that the methods are valid for quiescent-air conditions. As for the operation under the influence of external airflow, the validity of the methods remains yet to be quantified.

Characterization of the plasma-actuator performance under the influence of external airflow has been performed for the power consumption [8, 9] and net-force production [9]. Regarding the former, whilst Kriegseis *et al.*[8] determined a decreasing behaviour for free-stream velocities up to $M_\infty = 0.4$, Pereira *et al.*[9] experimental results indicated a constant behaviour for velocities up to $U_\infty = 60\,\mathrm{m/s}$. In addition, the net-force magnitude results revealed an increasing behaviour until $U_\infty = 30\,\mathrm{m/s}$ which then turn into a constant value for $U_\infty = 40$ m/s [9]. However, the impact of external flow on the body-force fields remains to be clarified. In the present study, the major objective is to study the time-averaged and phase-resolved body-force fields for different free-stream velocities and verify the validity of the N.S.E. and V.E. methods [5, 6]. The velocity information is acquired using Particle Image Velocimetry (PIV) measurements. The electrical quantities are recorded to quantify the power consumption behaviour [8, 9, 10]. Additionally, current measurements are performed to evaluate the plasma-discharge events and correlate with the phase-resolved forcing mechanism [7].

2. Body-force field determination

2.1. Method 1: Navier-Stokes momentum equation

The body-force field can be derived from the two-dimensional (2D) N.S.E. of a Newtonian incompressible fluid ($D\rho/Dt = 0$) with constant viscosity, see equations (1) [5]. The volume force term translates the plasma body-force field distribution $f_i(x, y)$.

$$\rho \frac{\partial u_i}{\partial t} + \rho u_j \frac{\partial u_i}{\partial x_j} = f_i - \frac{\partial p}{\partial x_i} + \mu \frac{\partial^2 u_i}{\partial x_j \partial x_j}. \tag{1}$$

Based on velocity-field measurements the convective, diffusive and unsteady terms can be easily determined. Nonetheless, the challenge of determining the pressure gradient experimentally in the presence of a plasma discharge is considerable [7], hence further assumptions are required. To deal with the additional unknown, Wilke [5] assumes the plasma-induced pressure gradient to be considerably small when compared with the body-force terms, thus it can be neglected ($f_i >> \partial p/\partial x_i$). The resulting equations for the body-force field determination are presented in the following equations (2) and (3) for x and y-direction, respectively.

$$f_x = \rho \frac{\partial u}{\partial t} + \rho \left(u \frac{\partial u}{\partial x} + v \frac{\partial u}{\partial y} \right) - \mu \left(\frac{\partial^2 u}{\partial x^2} + \frac{\partial^2 u}{\partial y^2} \right). \tag{2}$$

$$f_y = \rho \frac{\partial v}{\partial t} + \rho \left(u \frac{\partial v}{\partial x} + v \frac{\partial v}{\partial y} \right) - \mu \left(\frac{\partial^2 v}{\partial x^2} + \frac{\partial^2 v}{\partial y^2} \right). \tag{3}$$

2.2. Method 2: Vorticity equation

To overcome the problem of the unknown pressure gradient, Albrecht *et al.*[6] proposed a 2D V.E. approach. By determining the curl of the N.S.E., the pressure gradient term vanishes in a natural way. The expression is shown in equation (4).

$$\frac{1}{\rho} \left(\frac{\partial f_x}{\partial y} - \frac{\partial f_y}{\partial x} \right) = \rho \frac{\partial w}{\partial t} + u \frac{\partial w}{\partial x} + v \frac{\partial w}{\partial y} - \frac{\mu}{\rho} \left(\frac{\partial^2 w}{\partial x^2} + \frac{\partial^2 w}{\partial y^2} \right). \tag{4}$$

In this approach, the vorticity (w) is determined according to equation (5).

$$w = \frac{\partial v}{\partial x} - \frac{\partial u}{\partial y}. \tag{5}$$

Even though this approach discards the pressure gradient considerations, it considers both components of the force $f_x(x, y)$ and $f_y(x, y)$. Based on the plasma body-force field being dominated by the streamwise component, Albrecht *et al.*[6] assumes the curl of the force to be dominated by $\partial f_x/\partial y$. The final equation and subsequent integration is shown in equations (6) and (7).

$$\frac{1}{\rho} \frac{\partial f_x}{\partial y} = \rho \frac{\partial w}{\partial t} + u \frac{\partial w}{\partial x} + v \frac{\partial w}{\partial y} - \frac{\mu}{\rho} \left(\frac{\partial^2 w}{\partial x^2} + \frac{\partial^2 w}{\partial y^2} \right). \tag{6}$$

$$f_x = -\rho \int_{\infty}^{0} \left[\rho \frac{\partial w}{\partial t} + u \frac{\partial w}{\partial x} + v \frac{\partial w}{\partial y} - \frac{\mu}{\rho} \left(\frac{\partial^2 w}{\partial x^2} + \frac{\partial^2 w}{\partial y^2} \right) \right] dy. \tag{7}$$

Literature comprises two distinguished strategies to quantify the body-force field distribution of a plasma actuator: time-averaged or phase-resolved. Whilst the former relates with the averaged force production during a single discharge cycle, the latter describes the force mechanism at single phase positions. Previous experimental campaigns found the time-averaged body force to be quasi-steady i.e. the temporal term is found to almost null $\partial u_i/\partial t \approx 0$ [7]. On the contrary, the phase-resolved body force is dominated by the temporal term [7, 11]. Such an effect is a result of the highly unstable character of the plasma-discharge cycle [3, 12]. Accordingly, the temporal derivative of the velocity can be omitted for a time-averaged analysis. Furthermore, the assumptions of both N.S.E. and V.E. methods were found to be valid for a quiescent-air analysis. For instance, Kriegseis *et al.*[4] reported the resemblance of the body-force fields determined with the N.S.E. (2) and V.E. (7) to be a good indicator of the applicability of the methods. Moreover, the force is characterized by a positive volume-force generation in the vicinity of the exposed electrode. Similar findings were reported by Benard *et al.*[7]. The particular analysis of phase-resolved body-force distributions indicated an oscillatory behaviour of the force. On one hand, the positive-going half cycle comprises a mainly negative net volume force, on the other hand, the negative-going half cycle is found to produce a strong positive net force [7, 11].

3. Experimental setup and procedure

In the present study, planar high-speed PIV is used to determine the plasma-induced velocity field under influence of external airflow. The experiments are performed in a blower-type wind tunnel, at Karlsruhe Institute of Technology (KIT), Institute of Fluid Mechanics laboratory, that features optical access through a transparent test-section module made of *Plexiglas* (PMMA). The dimensions of the test section in length, width and height are $690 \times 320 \times 220\,\mathrm{mm}^3$, respectively. A flat plate with elliptic leading edge was installed, vertically centred within the test section, to provide support for the plasma actuator. The wind tunnel was set to operate at free-stream velocities up to $U_\infty = 20\,\mathrm{m/s}$.

3.1. AC-DBD plasma actuator and electrical setup

The geometrical characteristics and operational parameters are chosen according to the experiments of Kriegseis *et al.*[4] to ensure comparability. The exposed and encapsulated electrodes are made of copper and feature a width of 2.5 mm and 10 mm, respectively, and the dielectric is composed of 5 layers of Kapton tape with a total thickness of 0.3 mm. The length of the actuator is 150 mm in span ($z-$direction). The actuator is positioned in co-flow configuration (wall-jet along mean-flow direction), as depicted in figure 1, 57 mm downstream of the leading edge. A high-voltage generator (HVG) (Minipuls 2.1, GBS Elektronik GmbH) is used to supply the actuator with a sinusoidal waveform with peak-to-peak voltage of $V = 15\,\mathrm{kV}$ at an AC frequency $f = 10\,\mathrm{kHz}$.

The quantification of the electrical quantities and plasma-discharge events was performed by determining power consumption P and current I [10, 13]. The electric-charge method was used to determine the power consumption from the Lissajous figure ($Q - V$ cyclogram) [10, 13]. A monitor capacitor (capacitance $C = 22\,\mathrm{nF}$) was connected in series between the grounded electrode and ground. The voltage drop across the capacitor $V_C(t)$ and the electrode-voltage signal V were simultaneously acquired. The current measurements were performed by replacing the capacitor by a shunt resistor (resistance $R = 2.2\,\Omega$) [10, 7, 14]. The latter method is less accurate for determination of power consumption than the electric-charge method. However it is highly relevant with identifying the regimes of discharge collapse of the plasma [14]. For data acquisition an oscilloscope (Agilent InfiniiVision 2000 X-Series) with vertical resolution of 9 bit was used. The readings were taken with a sampling rate of 5 MSa/s at a maximum available length (25000 data points).

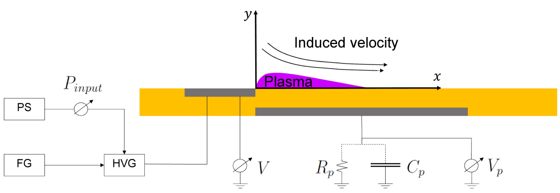

Figure 1: Schematic of the electrical setup including the high-voltage generator (HVG), function generator (FG), power supply (PS); power consumption and current measuring system: C_p capacitor, R_p resistor probe, V actuator voltage, V_p charge-probe voltage. Reproduced from Kriegseis *et al.*[4], fig. 1.

3.2. Particle image velocimetry

The high-speed PIV system comprises a Nd:YLF dual-cavity laser (Quantronix Darwin Duo) and a Photron Fastcam SA4 camera. The camera was placed outside the test section and was equipped with a Nikon AF micro Nikkor 200 mm f/4D IF-ID lens, and an extension of 108 mm total length was additionally applied, in order to obtain an appropriate object distance and high spatial resolution. The field-of-view (FOV) represents the $x - y$ plane and is permanently located in the mid-span ($z = 0$) of the flat plate, i.e., the x axis is along the mean-flow direction, y is the wall-normal coordinate and z is along the span. The camera imaged a FOV of $10 \times 4.5\,\mathrm{mm}^2$, yielding a spatial resolution of 96 px/mm. The coordinate-system origin $x = y = z = 0$ is the downstream edge of the exposed electrode on the surface of the plate. The flow was seeded with di-ethyl-hexylsebacat (DEHS) tracers, resulting in a Stokes number of $\leq 2.22 \times 10^{-2}$ for PIV measurements in the considered range of free-stream velocities of $U_\infty \leq 20\,\mathrm{m/s}$, hence the particles are expected to follow the flow motion with acceptable accuracy [15]. The present PIV system configuration is shown in figure 2.

Phase-resolved velocity data acquisition is divided in two sets of experiments, in which the discharge cycle is decomposed in 8 and 24 phase positions equally spaced in time. Accordingly, the phase-to-phase spacing yields $\Delta\phi = \pi/4$ and $\Delta\phi = \pi/12$, respectively. The PIV-acquisition parameters are depicted in table 3.2. The variables f_c, Δt_w and Δt_ϕ represent the camera frequency, pulse width and phase-to-phase time spacing, respectively.

Case	f_c (Hz)	Δt_w (μs)	$\Delta\phi$ (rad)	Δt_ϕ (μs)
CR	6.4	4	π / 4	12.5
FR	6.575	1	π / 12	4.167

Table 1: PIV-acquisition parameters. Note: The laser frequency is 0.5 f_c.

For each PIV run 5400 image pairs were recorded, converting into 675 and 225 image pairs per phase position for case CR and FR, respectively. The measurements were performed for free-stream velocities $U_\infty = [0, 5, 10, 15, 20]\,\mathrm{m/s}$. In case FR, three consecutive PIV runs were performed to obtain the same number of image pairs as for case CR. In addition, repeatability of the experiments was assured by taking three independent PIV runs for each tested free-stream velocity. Intermediate steps of U_∞ were introduced in case FR: $U_\infty = [2.5, 7.5]\,\mathrm{m/s}$. It is further to be mentioned that the base-flow velocity field was recorded for each setting of U_∞.

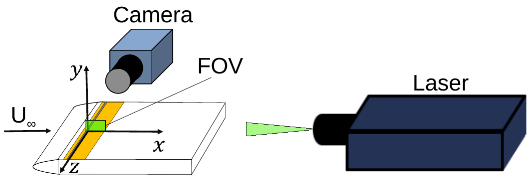

Figure 2: Particle image velocimetry system configuration comprising the high-speed camera, laser, field-of-view (FOV) and reference x, y, z axis with respect to the plasma actuator positioning.

3.3. Data processing and measurement uncertainty

The raw images were pre-processed, by applying a mean-image filter, in order to remove background noise and reflections. Subsequently, the mean-filtered images were processed with PIVview software in a multigrid/multipass approach, resulting in a final interrogation window size of $32 \times 16\,\mathrm{px}^2$ with overlaps of 75 and 50 %, respectively. The number of outliers was found to be $< 1\,\%$ which is in compliance with literature [15]. In order to ensure statistical significance of the velocity fields were carefully analysed by studying the convergence of the mean velocity in relevant regions [4, 11]. The results for each PIV measurements indicate that the velocity-fields converge within the available number of image pairs (not shown).

The accuracy of the PIV-velocity fields was evaluated with an uncertainty-quantification strategy for time-averaged velocity fields, reported in [16]. The strategy implies to determine the uncertainty of the time-averaged data, considering the standard deviation of the velocity field that includes fluctuation components and measurement errors. Individual analysis of the uncertainty associated to each PIV run with plasma actuation results in a maximum uncertainty of $< 2\%$ for quiescent air and $< 4\%$ for $U_\infty = 20\,\mathrm{m/s}$. The uncertainty of the remaining PIV runs is established within this range. For simplicity the uncertainty fields are not shown.

3.4. Base-flow boundary layer

The PIV-velocity fields of the base flow without plasma actuation were evaluated by means of boundary-layer thickness δ_{99} and shape factor H_{12} (see e.g. [17]) in the proximity of the plasma actuator. The shape factor H_{12} quantifies the boundary-layer condition. An additional parameter is introduced, hence to quantify the velocity felt by the plasma U_0 [9]. The parameter represents the average velocity of the velocity profile at the plasma location $x = 0\,\mathrm{mm}$. The extracted BL properties of the current experiment at $x = 0\,\mathrm{mm}$ are shown in table 2. The shape factor H_{12} for all free-stream velocities takes values larger than for the laminar Blasius flow. This is attributed to a decelerated flow regime - an adverse pressure gradient in the BL along the streamwise direction. The free-stream velocity in the experiments was limited to $U_\infty = 20\,\mathrm{m/s}$, in order to assure laminar flow in the measurement region. In order to quantify and further verify the base-flow adverse pressure gradient, the N.S.E. (2) was applied on the mean velocity field ($f_i = 0$). For low free-stream velocities, the maximum streamwise pressure gradient is found to be reasonably small, however for $U_\infty = 20\,\mathrm{m/s}$ the results show a control volume (CV) strip within the range of $y = 0.5\,\mathrm{mm}$ and $y = 1\,\mathrm{mm}$ height with a significant pressure gradient. Furthermore, the results indicate the same order-of-magnitude of the body-force field results determined by Kriegseis *et al.*[4] $\mathcal{O}(10^3)$. Hence, it might comprise the body-force determination with the N.S.E. method. Therefore, the adverse pressure gradient is taken into account when determining the body-force field with the N.S.E. method by subtracting the base-flow pressure gradient from the body force. It is noted that the body-force determination using the V.E. method should not be affected by the presence of an adverse pressure gradient.

Table 2: Boundary-layer flow properties at $x = 0$ without plasma actuation.

U_∞ (m/s)	δ_{99} (mm)	H_{12}	U_0 (m/s)
2.5	3.49	3.23	0.87
5	2.87	3.26	1.86
7.5	2.18	3.27	3.43
10	1.99	3.38	5.06
15	1.56	3.48	9.14
20	1.43	3.55	12.18

4. Results

4.1. Power consumption and current

The results of the electric characteristics of the present plasma-actuator configuration are shown in figures 3(a) and 3(b) for the power-consumption analysis and current, respectively.

The power consumption of the plasma actuator, shown in figure 3(a) for the considered free-stream velocities do not show a clear trend. However, the error bars indicate the estimated variation is within the standard deviation of the power-consumption analysis, thus the power consumption is considered to be virtually constant. The results for the power consumption resemble the findings of Pereira *et al.*[9] in co-flow configuration where the power consumption was found to be constant for free-stream velocities up to $U_\infty = 60\,\mathrm{m/s}$. On the other hand, Kriegseis *et al.*[8] reported a power consumption drop of about 3 % for $M_\infty = 0.1$, compared to quiescent-air value. The contrast between results can be attributed to higher-acquisition rate used by Kriegseis *et al.*[8] when compared to both the experiments of Pereira *et al.*[9] and the present study. Drops of power consumption in the order of 1 % require to capture the points near the peak-voltage locations, i.e. the two sharp ends of the $Q-V$ cyclogram, precisely. Furthermore, the linear law for thrust-power relation reported in literature indicates that such a variation of power consumption is expected to have a negligibly small effect on the volume integrated force [13, 14].

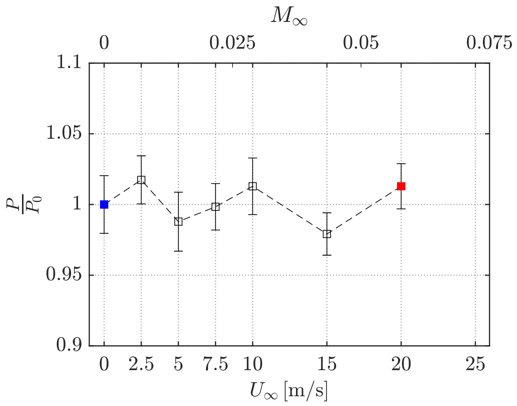

Figure 3: Relative power consumption based on P_0 quiescent air $U_\infty = 0\,\mathrm{m/s}$ for increasing free-stream velocity U_∞.

The current signals for quiescent air (blue data) and $U_\infty = 20\,\mathrm{m/s}$ (red data) superposed with the Lissajous figure, shown in figure 3(b) provide insight into the plasma-discharge events in both positive (lower branch) and negative-going half cycle (upper branch). Whilst the positive-going half cycle of the discharge features large current peaks (streamer discharge), the negative-going half cycle is expected to produce smaller current peaks (glow discharge) [12]. In the present study, the positive-going half cycle presents only weakly enhanced current peaks when compared to the negative counterpart, with the negative-going half cycle being somewhat irregular which is in contradiction with literature [7, 12, 14]. This might be attributed to the lower vertical resolution compared to the experiment by Benard *et al.* [7]. Moreover, the results clearly show the regions where the discharge quenches before entering the subsequent discharge regime by the absence of current peaks (dash line). The discharge collapsed region can be identified immediately after the end of both positive- and negative-going half cycle, corresponding to the phase positions $\phi = \pi/2$ and $\phi = 3\pi/2$, respectively. Subsequently, the discharge enters the 'dark period', i.e. no plasma formation. The discharge collapsed region is within the phase positions $6/12\pi \leq \phi \leq 10/12\pi$ and $19/12\pi \leq \phi \leq 22/12\pi$ for positive- and negative-going half cycle. It is noted that as the current is found to be null, the integral value of the force F_x is expected to be identical to zero. By comparing both current signals for quiescent air and $U_\infty = 20$ m/s, the onset in each half-cycle is found for a constant phase position, independently of the free-stream velocity.

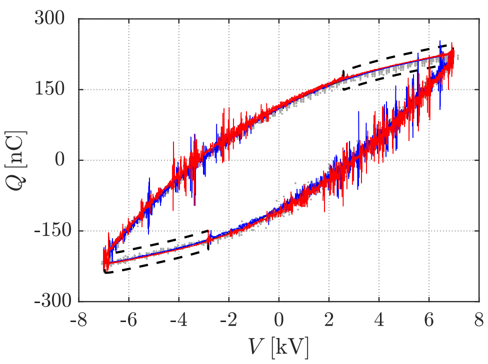

Figure 4: Lissajous figure ($Q-V$ cyclogram) in quiescent air $U_\infty = 0\,\mathrm{m/s}$ (black solid line) and current signal I for quiescent air $U_\infty = 0\,\mathrm{m/s}$ (blue data) and $U_\infty = 20\,\mathrm{m/s}$ (red data).

4.2. Time-averaged body force

The spatial distribution of the produced volume force by the plasma actuator under quiescent-air conditions and in the presence of external airflow is shown in figures 5(a)-(f), where the left and right column represent the body-force fields determined with the N.S.E. and V.E. method, respectively. The resemblance of the body-force fields in quiescent air determined with the N.S.E. (2) and V.E. (7) show a good correlation, see figures 5(a) and 5(b). Previous experimental campaigns also reported similar findings and concluded that both methods lead to trustful results in quiescent air [4, 7]. It is however to be noticed that a minor difference between the body-force fields, shown in figures 5 (a) and (b), is found downstream of the exposed electrode where a negative-force contribution appears. The analysis of the source terms contribution indicates the convective term as the source of the negative force region. As the convected fluid elements evolve downstream, viscous effects start to appear, hence decelerating the plasma-induced airflow gradually. Accordingly, the velocity gradient $\partial u/\partial x$ becomes a negative contribution to the body-force field [4]. Such an effected appears to be more pronounced with the N.S.E. (2). In contrast, the region of maximum magnitude near the exposed electrode ($x = 0\,\mathrm{mm}$) appears to be larger when estimated with the V.E. (7).

The impact of external flow on the body-force field $f_x(x, y)$ is analysed for free-stream velocities $U_\infty = [10; 20]$ m/s for both approaches on figures 5(c)-(f). The time-averaged force fields in the left column (N.S.E. model) for increasing free-stream velocity U_∞ (top to bottom) show a significant impact of external airflow. The dominant region of the force distribution is decisively decreased as the external-airflow velocity is increased up to $U_\infty = 20\,\mathrm{m/s}$. On top of the bulk of the force, a negative volume-force region appears ($x = 0\,\mathrm{mm}$), which becomes more pronounced for higher free-stream velocity. At the same time, a separated region from the most significant region of the body-force field that yields a positive net force becomes noticeable, see for instance figure 5(c) at $x \approx 0\,\mathrm{mm}$ and $y \approx 0.5\,\mathrm{mm}$. Regarding the V.E. method, the results are shown in figures 5(d) and 5(f) for increasing U_∞. In contrast to the results determined with the N.S.E. (2), the estimation with the V.E. (7) indicate this method to be more robust. Direct comparison with quiescent-air conditions, indicates that the impact of the external flow on the plasma body-force field appears to extend only to a minor part of the spatial distribution for free-stream velocities up to $U_\infty = 10\,\mathrm{m/s}$. A remarkable effect is however evidenced, on one hand, near in the vicinity of the exposed electrode the area of higher magnitude seems to be larger. On the other hand, the streamwise extend appears to shrink. For higher free-stream velocities $U_\infty = 20\,\mathrm{m/s}$, shown in 5(f), the region of strong positive force increases in magnitude and area. Nonetheless, the body-force field general features remain unchanged.

The global impact of the momentum-transfer ability of the actuator on F_x often termed 'Thrust' is determined by integrating the plasma body-force over a CV. In previous reports, a 10 %-isoline of the force $f_x(x, y)$ was defined as a relevant integration domain [4]. Taking into account the significant changes of the body-force field with increasing free-stream velocity, this strategy would not characterize the net-force production within the same region, hence the results for different free-stream velocities would not be comparable. Accordingly, the body-force field $f_x(x, y)$ is integrated over a rectangular CV defined by the limits $-1.5 \leq x \leq 6\,\mathrm{mm}$ and $0 < y \leq 2\,\mathrm{mm}$, see figure 8. For quiescent air conditions, the results evidenced the compliance between both N.S.E. and V.E. methods. Specifically, the N.S.E. approach force integral F_x is estimated to be only 1.5% larger in comparison with the V.E. method. As for the influence of external flow, the force magnitude estimated with the N.S.E. method indicates a significant impact. For instance, reduction in the estimated thrust of about 40% is already determined for free-stream velocity $U_\infty = 2.5\,\mathrm{m/s}$. For higher free-stream velocities $U_\infty \geq 15\,\mathrm{m/s}$, the continuously decreasing trend leads to negative values of the net force F_x. On the contrary, the V.E. exhibits a decrease of about 17% from quiescent air to laminar BL operation at free-stream velocity $U_\infty = 2.5\,\mathrm{m/s}$, which then tends to converge to a rather constant value for free-stream velocities up to $U_\infty = 15\,\mathrm{m/s}$. A mild increase is detected for $U_\infty = 20\,\mathrm{m/s}$. In general, the small variations of power consumption anticipated a rather constant electrical-to-mechanical conversion, hence the actuator is expected to produce the almost amount of net force for the considered free-stream velocities. Accordingly, the analysis of the thrust production appears to indicate that the V.E. method leads to reasonable results in the presence of external flow. In contrast, the N.S.E. method seems to be significantly influenced by the negligible pressure gradient $\partial p/\partial x$, which is an indicator that the assumption leads to an oversimplification. At this point, the subtraction of the base-flow adverse pressure gradient is questionable. This is because no physical phenomenon associated with imposing an external airflow on a AC-DBD plasma actuator may explain the change in direction of the plasma net-force production.

4.3. Phase-resolved force

The phase-resolved body-force field determination strategy enabled to quantify the force production in 24 phase positions over a single discharge cycle. Due to high resolution of the discharge cycle, the results are analysed only for 3 out of 24 phase positions. Accordingly, the phase positions are selected according to the estimated minimum $\phi = \pi/12$ and maximum $\phi = 5\pi/4$ net force production, and an additional phase position on the positive-going half cycle $\phi = \pi/3$. The body-force fields determined with the N.S.E. (equation 2) and V.E. (equation 7) are shown for free-stream velocities $U_\infty = [0, 20]\,\mathrm{m/s}$ in figures 6(a)-(l). The first and second row correspond to the N.S.E. method for quiescent-air conditions and $U_\infty = 20\,\mathrm{m/s}$, whereas the third and fourth to the V.E. method for quiescent-air conditions and $U_\infty = 20\,\mathrm{m/s}$

The results determined with both methods clearly indicate the oscillating behaviour of the discharge cycle. Whilst the positive-going half cycle is found to produce a mainly negative volume force, the negative-going half cycle is responsible for generating a mainly positive volume force. Previous experimental studies determined the same behaviour of the phase-resolved body-force fields [7, 11]. Regarding the N.S.E. method, the body-force production during the positive-going half cycle seems to present a slight impact of the external flow at free-stream velocity $U_\infty = 20\,\mathrm{m/s}$ when compared to quiescent air (see fig. 6(a),(e); fig. 6(b),(f)). The results indicate that for $U_\infty = 20\,\mathrm{m/s}$, the

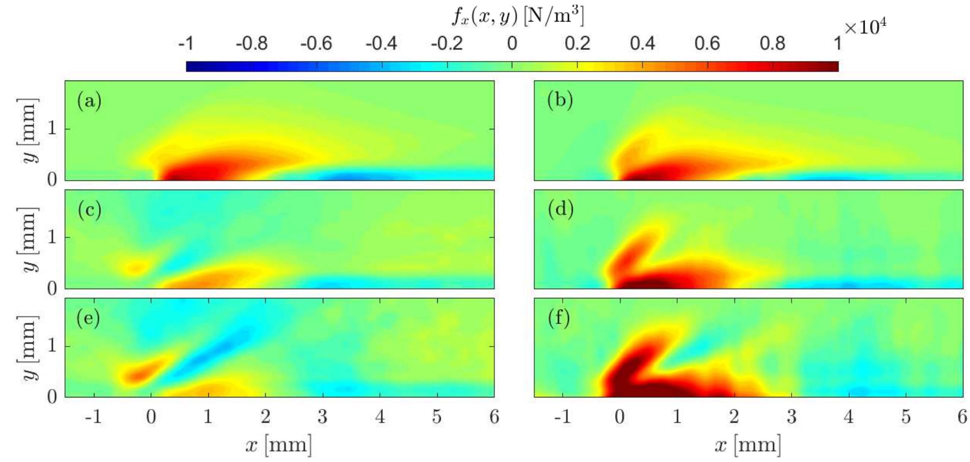

Figure 5: Plasma time-averaged horizontal body-force distribution $f_x(x, y)$ determined according to N.S.E. (equation 2) (left column) and V.E. (right column) (equation 7) for increasing free-stream velocity $U_\infty = [0, 10, 20]$ m/s (top to bottom).

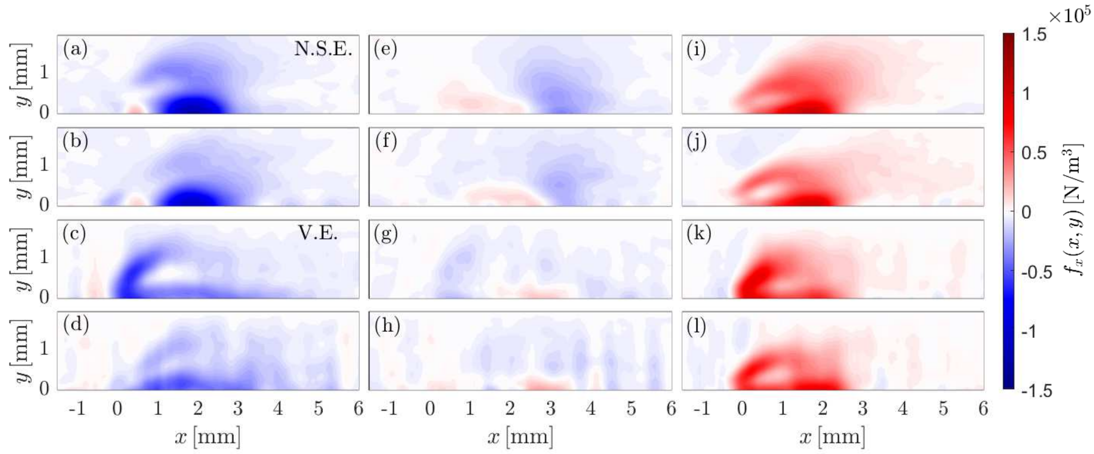

Figure 6: Plasma phase-resolved body-force distribution $f_x(x, y)$ determined according to N.S.E. (equation 2) (first and second row) and V.E. (third and fourth row) (equation 7) for increasing free-stream velocity $U_\infty = [0, 20]$ m/s (top to bottom for each case).

region where the body-force magnitude is larger ($x = 2$ mm), becomes smaller in height. Nonetheless, the general features appear to remain unchanged. For instance, the positive volume generation immediately downstream the exposed electrode ($x \approx 0.2$ mm) and higher magnitude region can be clearly identified. For the negative-going half cycle, the impact seems to be slightly higher, with an oval-like shape centred at $x \approx 0.5$ mm and $y \approx 0.2$ mm becoming more pronounced when operating with free-stream velocity (see fig. 6(i); fig. 6(j)). Additionally, the dominant region of the positive volume-force generation appears to be diminished.

In contrast, the body-force fields determined with the V.E. method indicate a higher degradation during the positive-going half cycle in the presence of external flow. Direct comparison between quiescent-air conditions and $U_\infty = 20$ m/s indicate a significant impact of external flow (see fig. 6(c),(g); fig. 6(d),(h)). On the other hand, the negative-going half cycle seems to be more robust to the presence of external airflow (see fig. 6(k); fig. 6(l)).

The comparison between both strategies indicates that the most significant features of the phase-resolved body-force field can be identified regardless of the method during the negative-going half cycle (see fig. 6(i)-(l)). For the positive counterpart, a divergence trend is determined. Whilst the N.S.E. (equation 2) body-force field evidences a slight impact, the results determined with the V.E. (equation 7) appear to be more sensitive. In addition, when comparing both methods, the results indicate considerable different spatial distribution of the force (see fig. 6(a)-(d)).

The phase-resolved net-force production is quantified by integrating the body-force field over the defined CV. The results are shown in figures 7(a) and 7(b) for the N.S.E. and V.E. method, respectively. The former, during the positive-going half cycle indicates an impact of the external airflow only for high free-stream velocities $U_\infty \geq 15\,\mathrm{m/s}$. The effect is clearly identified at the minimum location $\phi = \pi/12$. During the negative-going half cycle, the effect is more pronounced, with a rather constant decrease being evidenced for free-stream velocities up to $U_\infty = 10$ m/s, whilst a larger drop of about 38% is determined for $U_\infty \geq 15$ m/s. The results determined with the V.E. method indicate a continuously growing impact during the positive-going half cycle as free-stream velocity is increased. In contrast, the negative-going half cycle appears to be more robust.

The current signal (grey) is added to the plots in order to evaluate the relation between the discharge events and forcing mechanism, see figures 7(a) and 7(b). As the current becomes null, i.e., there is no plasma discharge, the net force is expected to be identical to zero. By comparing both discharge collapse regions and corresponding net force production, the results seem to estimate a virtually null force after the positive-going half cycle. Even though, such a conclusion seems to be more trustful when considering the V.E. method. During the second discharge collapse region, the estimated force features negative values, which are found to be larger when estimated with the N.S.E. method. In addition, with the N.S.E. approach the results appear to depend on the free-stream velocity whereas the V.E. method seems to be more robust.

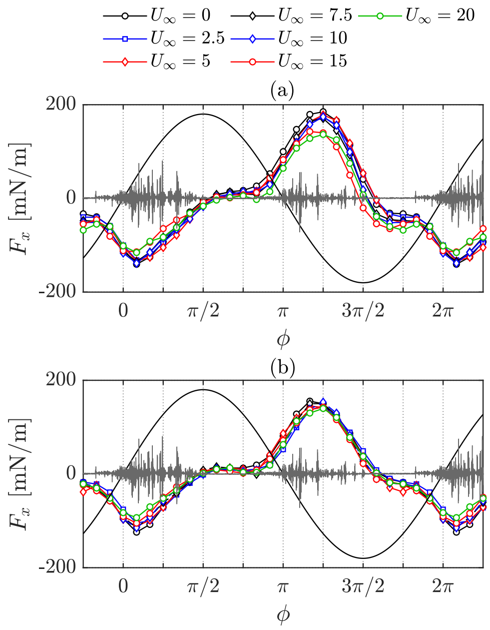

Figure 7: Integrated value of the phase-resolved streamwise body-force field Fx according to (a) N.S.E. (equation 2); (b) V.E. (equation 7). Current signal in grey.

5. Discussion

5.1. Role of unknown pressure gradient

The extensive experimental study on the time-averaged and phase-resolved body-force fields shed light into the validity of the N.S.E. and V.E. methods. The results in quiescent-air conditions for the time-averaged body force appear to indicate that both methods lead to trustful results. For instance, this is evidenced by the compliance between the body-force magnitude and spatial distribution determined with both methods, see figures 5(a) and 5(b). On the other hand, the phase-resolved analysis indicates a slightly divergent body-force estimation between both approaches. The spatial distribution was found to be mildly changed and the N.S.E. integral value seems to estimate a larger net force. Nonetheless, it seems reasonable to assume that both methods are valid for quiescent-air conditions.

In the presence of external airflow, the time-averaged results show a divergent behaviour between both methods. With the N.S.E. method, the body-force field dominant region of positive net force is significantly diminished in height and length. In addition, a negative volume force on top of the bulk of the plasma gradually grows as external-airflow velocity is increased. In contrast, the body-force fields determined with the V.E. approach, shows robust for free-stream velocities up to $U_\infty = 10\,\mathrm{m/s}$. For higher free-stream velocity $U_\infty = 20\,\mathrm{m/s}$, the results indicate a mild impact of the external flow on the body force. The volume-integrated force analysis F_x indicates a virtually constant net force determined with the V.E. method when operating with external flow, whereas the N.S.E. shows a decisively decreasing behaviour which results in negative values for $U_\infty \geq 15\,\mathrm{m/s}$. Regarding the phase-resolved body-force fields, an evaluation of the impact of external flow on the force is more complex. On one hand, the negative-going half-cycle shows only a slight impact for high free-stream velocity for both methods, compared to quiescent air. On the other hand, the positive-going half cycle is found to present only a minor impact with the N.S.E. whereas the results determined with the V.E. approach show a significant impact.

Correlation with the power consumption anticipates a constant net-force output for the virtually constant power consumption results, see section 4.1 [13, 14]. On one hand, the integrated volume-force determined with the V.E. resembles such a behaviour. On the other hand, the results obtained with the N.S.E. do not correlate with the expected electrical-to-mechanical conversion. As for the N.S.E. method, assuming the base-flow adverse pressure gradient being unchanged with and without plasma actuation, the varying results for different free-stream velocities obtained with the N.S.E. method are attributed to the plasma-induced pressure gradient, hence it implies an oversimplification of the method. In addition, it should be noted that this conclusion indicates that the plasma actuator is responsible for producing a pressure gradient and further investigations are required to uncover this.

5.2. Reproducibility of body-force fields

Analysis of the reproducibility of the body-force fields is investigated in figure 8 based on the time-averaged force production, according to the N.S.E. (blue data) and the V.E. (black data) method. The squares and the circles depict the data of the first and second set of experiments with phase resolutions of 8 and 24 phases per cycle, respectively. In addition, the average of the resultant forces of each single measurements is calculated and error bars are included to visualize the uncertainty of the measurements. Both experiments show consistent trends and magnitudes for the integral force F_x within the uncertainty band. The compliance between both experiments is considerable, taking into account the divergence of the results from both models that lead to orders-of-magnitude change, with even a change of the sign. One might argue that the scatter is rather large for some free-stream velocities. However, being able to reproduce the trend is already an important indicator of the accuracy of the measurements. The range in which the results are comprised is dependent of the plasma actuator assembly and PIV calibration, which might induce slightly different measurements. Furthermore, it should be noticed that the reproducibility not only verifies the accuracy of the measurements but also indicates that two different plasma actuators operating in the same conditions are able to produce similar body force. Consequently, the reproducibility of the body-force results justifies a solid interpretation of the results on the force distributions and magnitude.

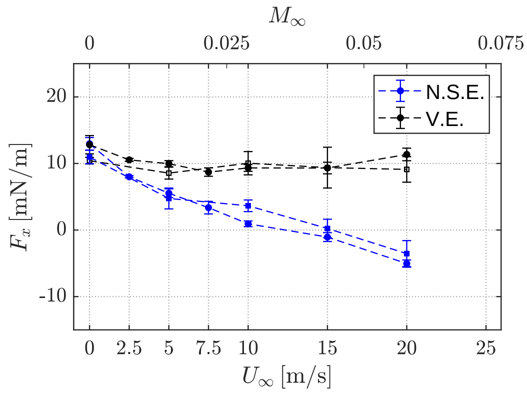

Figure 8: Reproducibility of the body-force results determined according to NSE (2) (blue data) and V.E. (7) (black data); solid squares represent the first set of experiments and empty circles the second.

6. Conclusions

In the present experimental investigation, the electrical and mechanical characteristics of an AC-DBD plasma actuator were determined in presence of an external laminar BL flow. Regarding the electrical quantities, the power consumption and current signal analysis led to a virtually constant power consumption of the plasma actuator for flow speeds up to $U_\infty = 20\,\mathrm{m/s}$ and indicated that the regimes of discharge collapse are located at the same phase positions regardless of the operating free-stream velocity (sec.4.1) [10, 13]. As for mechanical characterization, phase-resolved velocity information were acquired with high phase resolution of 24 phases per discharge cycle to derive the body-force fields, using the N.S.E. and V.E. methods (sec.4.2 & 4.3) [5, 6]. The insights into the phenomena occurring over a discharge-cycle can be summarized as follows:

- The N.S.E. method introduced by Wilke [5] relies on a negligibly small pressure gradient due to the plasma discharge, however this assumption is an oversimplication of the problem when considering the presence of external airflow. The volume integrated time-averaged force F_x showed a decisively decreasing progression, which results in negative values of the force for $U_\infty > 15\,\mathrm{m/s}$. Such a behaviour can only be attributed to a plasma-induced pressure gradient, neglected in the calculations, as no physical phenomenon associated with imposing an external airflow on an AC-DBD plasma actuator may explain the change in direction of the plasma-force production.

- The body-force model by Albrecht *et al.*[6], in contrast, relies on the assumption of a negligibly force gradient $\partial f_y/\partial x$, thus it results only in the wall-parallel component of the force $f_x(x, y)$. In the present study, the body-force field estimation appears to determine only a mild variation of the integral value of the force F_x when operating with external flow. However, the results tend to converge to a rather constant value for free-stream velocities up to $U_\infty = 15\,\mathrm{m/s}$. It is further to be noted that the integral-force magnitude was found to be within a determined order-of-magnitude, correlating with the power consumption analysis of the actuator. Nonetheless, the problem of the unknown wall-normal force $f_y(x, y)$ remains to be solved in future.

- The reliability of both the plasma actuator (in terms of manufacturing and operation) and the force-determination strategy has been demonstrated by the reproducibility study which justifies a solid interpretation of the results on the force distributions and magnitudes.
- First PIV experiments to derive the body force from velocity fields in external laminar BL flow.

Acknowledgements

First and foremost, I would like to thank the opportunity to join the research team of experimental fluid mechanics at Karlsruhe Institute of Technology (KIT), specially to Dr. Ing. Jochen Kriegseis and Msc. Marc Hehner. I would also like to thank my supervisor Prof. Ricardo Pereira. Special thanks to my family and friends.

References

[1] Louis N. Cattafesta and Mark Sheplak. Actuators for active flow control. *Annual Review of Fluid Mechanics*, 43(1):247–272, 2011.

[2] Jérôme Jolibois, Maxime Forte, and Éric Moreau. Application of an ac barrier discharge actuator to control airflow separation above a naca 0015 airfoil: Optimization of the actuation location along the chord. *Journal of Electrostatics*, 66(9):496 – 503, 2008.

[3] Thomas Corke, Martiqua L. Post, and Dmitry M. Orlov. Sdbd plasma enhanced aerodynamics: concepts, optimization and applications. *Progress in Aerospace Sciences*, 43:193–217, 10 2007.

[4] J Kriegseis, C Schwarz, C Tropea, and S Grundmann. Velocity-information-based force-term estimation of dielectric-barrier discharge plasma actuators. *Journal of Physics D: Applied Physics*, 46(5):055202, jan 2013.

[5] B Wilke. *Aerodynamische strömungssteuerung mittels dielektrischen Barriereentladungs-Plasmaaktuatoren*. PhD thesis, Technische Universität Darmstadt, DLR, 2009.

[6] Thomas Albrecht, Tom Weier, Gunter Gerbeth, Hans Metzkes, and Jörg Stiller. A method to estimate the planar, instantaneous body force distribution from velocity field measurements. *Physics of Fluids - PHYS FLUIDS*, 23, 02 2011.

[7] N Benard, A Debien, and E Moreau. Time-dependent volume force produced by a non-thermal plasma actuator from experimental velocity field. *Journal of Physics D: Applied Physics*, 46(24):245201, may 2013.

[8] J. Kriegseis, S. Grundmann, and C. Tropea. Airflow influence on the discharge performance of dielectric barrier discharge plasma actuators. *Physics of Plasmas*, 19(7):073509, 2012.

[9] Ricardo Pereira, Daniele Ragni, and Marios Kotsonis. Effect of external flow velocity on momentum transfer of dielectric barrier discharge plasma actuators. *Journal of Applied Physics*, 116:103301–103301, 09 2014.

[10] David Ashpis, Matthew Laun, and Elmer Griebeler. *Progress toward Accurate Measurements of Power Consumption of DBD Plasma Actuators*. 2012.

[11] M Kuhnhenn, Bernhard Simon, I Maden, and Jochen Kriegseis. Interrelation of phase-averaged volume force and capacitance of dielectric barrier discharge plasma actuators. *Journal of Fluid Mechanics*, 809, 12 2016.

[12] Eric Moreau. Airflow control by non-thermal plasma actuators. *Journal of Physics D: Applied Physics*, 40(3):605–636, jan 2007.

[13] J. Kriegseis, S. Grundmann, and C. Tropea. Power consumption, discharge capacitance and light emission as measures for thrust production of dielectric barrier discharge plasma actuators. *Journal of Applied Physics*, 110(1):013305, 2011.

[14] Antoine Debien, Nicolas Benard, and Eric Moreau. Streamer inhibition for improving force and electric wind produced by DBD actuators. *Journal of Physics D: Applied Physics*, 45(21):215201, may 2012.

[15] Markus Raffel, Christian E. Willert, Steven Wereley, and Jürgen Kompenhans. *Particle Image Velocimetry*. Springer-Verlag Berlin Heidelberg, 2 edition, 2007.

[16] Andrea Sciacchitano and Bernhard Wieneke. Piv uncertainty propagation. *Measurement Science and Technology*, 27:084006, 08 2016.

[17] Vasco de Brederode. *Aerodinâmica Incompressível: Fundamentos*. IST Press, 2014.